Mechanistic Modeling of Water-Alternating-Gas Injection and Foam-Assisted Chemical Flooding for Enhanced Oil Recovery

Janssen, Martijn T.G.; Torres Mendez, Fabian A.; Zitha, Pacelli L.J.

DOI
10.1021/acs.iecr.9b06356

Publication date
2020

Document Version
Final published version

Published in
Industrial and Engineering Chemistry Research

I&EC research
Industrial & Engineering Chemistry Research

pubs.acs.org/IECR

Article

Mechanistic Modeling of Water-Alternating-Gas Injection and Foam-Assisted Chemical Flooding for Enhanced Oil Recovery

Martijn T. G. Janssen,* Fabian A. Torres Mendez, and Pacelli L. J. Zitha

Cite This: *Ind. Eng. Chem. Res.* 2020, 59, 3606−3616

Read Online

ACCESS | Metrics & More | Article Recommendations | Supporting Information

ABSTRACT: History-matching of core-flood experimental data through numerical modeling is a powerful tool to get insight into the relevant physical parameters and mechanisms that control fluid flow in enhanced oil recovery processes. We conducted a mechanistic numerical simulation study aiming at modeling previously performed water-alternating-gas and foam-assisted chemical flooding core-flood experiments. For each experiment, a one-dimensional model was built. The obtained computed tomography scan data was used to assign varying porosity, and permeability, values to each grid block. The main goal of this study was to history-match measured phase saturation profiles along the core length, pressure drops, produced phase cuts, and the oil recovery history for each of the experiments conducted. The results show that, to obtain a good match for the water-alternating-gas experiment, gas relative permeability needs to be reduced as a function of injection time due to gas trapping. The surfactant phase behavior, for the aid of foam-assisted chemical flooding, was successfully simulated and its robustness was verified by effectively applying the same phase behavior model to the two different salinity conditions studied. It resulted in the oil mobilization, through the injection of a surfactant slug, being properly modeled. The mechanistic simulation of foam using the steady-state foam model built in UTCHEM proved inadequate for the mechanistic modeling of a foam drive in the presence of oil. An alternative heuristic approach was adopted to overcome this limitation.

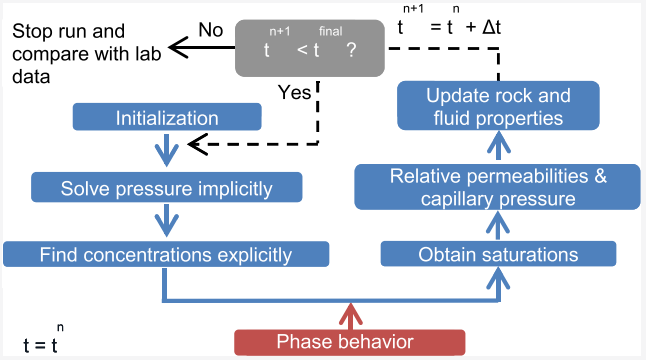

1. INTRODUCTION

One of the major concerns regarding the energy supply and consumption in today's world is that the global oil demand will outrun the world's oil production in the near future as oil demand continues to remain high while oil production from many giant, mature, oil fields is declining.[1] In addition to the expectation that the likelihood of discovering new, large, oil fields is minimal, this emphasizes the significance of developing novel techniques that can enhance oil production from mature oil fields: enhanced oil recovery (EOR) methods.

Gas injection is a commonly used EOR technique. One of the major drawbacks related to gas flooding is the unfavorable mobility ratio between the injected gas and the displaced fluids. It might result in viscous instabilities that yield viscous fingering, gas channeling in high-permeability streaks, and gravity segregation, all leading to an early breakthrough of gas.[2−6]

To overcome the aforementioned deficiencies related to continuous gas injection, one might inject the gas phase in slugs alternated by slugs of water, i.e., water-alternating-gas (WAG) flooding.[7−9] Nevertheless, gravity segregation may also occur during WAG injection, resulting once again in an early breakthrough of the gas phase.[6]

An alternative method for improving gas sweep efficiency, thus delaying its breakthrough time, is foaming of the gas. Foam is able to reduce gas mobility greatly by trapping the gas in separate gas bubbles within a continuous aqueous phase.[10−15] Foam stability is primarily a function of the thickness of thin liquid films, i.e., lamellae, that separate the gas bubbles within the foam texture.[5,16,17] The lamellae are stabilized by selected surfactants that are present in the liquid phase.

Aside from a favorable sweep efficiency, i.e., volume fraction of the reservoir that is contacted by the injectants, a promising displacement efficiency, i.e., fraction of oil mobilized in the swept region, is required as well to perform a successful chemical EOR project. This might be achieved by adding carefully formulated surfactants to the aqueous phase prior to injection. The surfactants induce mobilization of residual oil trapped by capillary forces after waterflooding.[18−21] They do so by effectively reducing the oil−water (o/w) interfacial tension (IFT) by multiple orders of magnitude. The latter yields a drastic increase in capillary number. The extent to which a constant surfactant concentration, at a fixed pH, can lower the o/w IFT of a specific oil−water−surfactant system is essentially controlled by the salinity of the water phase.[16,22,23] At under-

Received: November 19, 2019
Revised: January 27, 2020
Accepted: January 28, 2020
Published: January 28, 2020

https://dx.doi.org/10.1021/acs.iecr.9b06356
Ind. Eng. Chem. Res. 2020, 59, 3606−3616

Table 1. Overview of the Core-Flood Experiments Simulated in This Study[a]

simulation	procedure	experiment to history-match	information on chemicals and core samples	information on experimental setup and procedure
1	WAG	exp. 3 in ref 9	sections "chemicals" and "core samples" in ref 9	sections "experimental setup" and "experimental procedure" in ref 9
2	CF	ASF0 in ref 26	sections "chemicals" and "core samples" in ref 26	sections "experimental setup" and "experimental procedure" in ref 26
3	FACF	ASF1 in ref 26	sections "chemicals" and "core samples" in ref 26	sections "experimental setup" and "experimental procedure" in ref 26
4	FACF	ASF2 in ref 26	sections "chemicals" and "core samples" in ref 26	sections "experimental setup" and "experimental procedure" in ref 26
5	FACF	ASF3 in ref 26	sections "chemicals" and "core samples" in ref 26	sections "experimental setup" and "experimental procedure" in ref 26
6[b]	FACF	exp. 5 in ref 9	sections "chemicals" and "core samples" in ref 9	sections "experimental setup" and "experimental procedure" in ref 9

[a]CF refers to chemical flooding, i.e., extended surfactant slug injection. [b]In simulation 6, the drive foam part was not modeled since we aimed to compare oil mobilization by slug injection at under-optimum salinity (simulation 3) to injection at (near-)optimum salinity (simulation 6).

optimum salinity conditions, an oil-in-water microemulsion (ME) coexists with excess oil (type II− system). However, at over-optimum salinity, a water-in-oil microemulsion is in equilibrium with excess water (type II+ system). An optimum salinity range (type III system), where a distinct microemulsion coexists with excess oil and water, can be found in between the type II− and type II+ systems. Here, the systems show ultralow o/w IFTs.

Foam-assisted chemical flooding (FACF) combines the injection of a surfactant slug, for mobilizing residual oil, with foam generation for drive mobility control, thus obtaining favorable sweep efficiency.[9,20,24−26] In a well-designed FACF, the surfactant slug provides an ultralow o/w IFT and adequately low slug mobility, mobilizing previously trapped residual oil and thus leading to the development of an oil bank. Surfactant slug mobility, which is a function of its viscosity and relative permeability, is relevant as it controls the part of the reservoir being contacted by the slug, determining the amount of oil that can potentially be mobilized from the reservoir. The latter has been pointed out by several studies on fractional flow analysis for chemical EOR processes.[54,55] Subsequent to slug injection, the injection of a foam drive ensures good mobility control for displacement of the oil bank.

Previously, we reported on an experimental study on WAG injection in Bentheimer sandstone cores.[9] Experimental results suggest that, when applying WAG flooding instead of continuous immiscible gas injection, one can increase the ultimate oil recovery due to an increased sweep efficiency as a result of the introduction of a trapped, i.e., immobile, gas saturation.[9]

In our other recent work, we presented a laboratory study on FACF where we addressed the effect of the drive foam quality on oil bank propagation in an FACF process conducted at under-optimum salinity.[26] It shows that the oil bank displacement, during an FACF process at model-like conditions, was most stable at the lowest foam quality investigated. The effect of the surfactant slug salinity on the efficiency of FACF in a model-like setting is discussed in our other, previously published, work.[9] The results indicate that the increase in displacement efficiency, when performing FACF at (near-)optimum salinity conditions compared to under-optimum salinity, led to the formation of a more uniform and elongated oil bank. Moreover, the ultimate oil recovery could be increased with 15 ± 5% of the oil initially in place (OIIP) when conducting FACF at (near-)optimum salinity conditions instead of under-optimum salinity.[9] Note that the terminology used in our earlier work[9,26] differs from the terminology used here [alkaline−surfactant−foam (ASF) flooding is identical to FACF].

The goal of this study was the mechanistic modeling of WAG and FACF core-flood experiments presented in our earlier work.[9,26] More specifically, we aimed to capture the underlying mechanisms that drive each of the aforementioned EOR processes. Simulation results were compared with experimental results to see whether we can validate the conclusions, and suggestions, made based on the experimental studies. For this purpose, a three-dimensional chemical flooding simulator for multiphase and multicomponent systems was used: the UTCHEM simulator. The FACF core-floods presented earlier[9,26] were modeled by including the surfactant phase behavior as a function of salinity, fluid rheology, capillary desaturation of oil, gas mobility reduction due to foam generation, and potential essential geochemical reactions that occurred in the sandstone core. All simulations were performed under a one-dimensional configuration.

2. MATERIALS AND METHODS

2.1. WAG Injection. The first experiment that was simulated using the UTCHEM simulator is the WAG experiment (exp. 3 in our earlier work).[9] Related chemicals, physical properties of the sandstone core, experimental setup, and experimental procedure are described in our previous work.[9] Table 1 provides details regarding where the aforementioned information can be found.

2.2. FACF. The second simulated experiment is the extended surfactant slug injection experiment (ASF0 in our previous work).[26] Simulations 3−5 represent experiments ASF1−ASF3 in our earlier published material.[26] Information on the chemicals, sandstone samples, and experimental setup and procedure is described in detail elsewhere.[26] More specifics on where the abovementioned information can be obtained are shown in Table 1.

The final experiment that was modeled in this study is FACF at (near-)optimum salinity conditions (exp. 5 in our previous work).[9] Related chemical and core samples, which were used for successfully conducting the experiment, and corresponding details on the experimental setup and procedure are shown in our earlier work.[9] Table 1 presents an overview of all of the simulations conducted in this study.

2.3. UTCHEM Simulator. Recently, only a few three-phase chemical flooding simulators have been developed that are able to model the oil−water−microemulsion equilibrium state.[27−30] These simulators are suitable for modeling EOR applications

https://dx.doi.org/10.1021/acs.iecr.9b06356
Ind. Eng. Chem. Res. 2020, 59, 3606−3616

such as surfactant flooding and alkaline−surfactant−polymer injection. Well-known commercial reservoir simulators like ECLIPSE, STARS, INTERSECT, and VIP are only capable of modeling three-phase oil−water−gas conditions, appropriate for simulating gas flooding and WAG.[31] However, to capture all physical mechanisms related to FACF, a four-phase oil−water−gas−microemulsion equilibrium model is required: UTCHEM. The results presented in this study were acquired using UTCHEM-2017.3, which is a finite-difference, implicit pressure, explicit concentration, i.e., IMPES type, formulation that was developed at the Center for Petroleum and Geosystems Engineering at The University of Texas in Austin, TX.[32]

To simulate chemical EOR with gas, UTCHEM couples a black-oil model (for oil−water−gas systems) with Hand's rule for microemulsion phase behavior (oil−water−microemulsion systems). Hand's rule[33] is used to calculate the oil−water−surfactant phase behavior as a function of salinity and concentrations. Figure 1 presents a schematic that illustrates

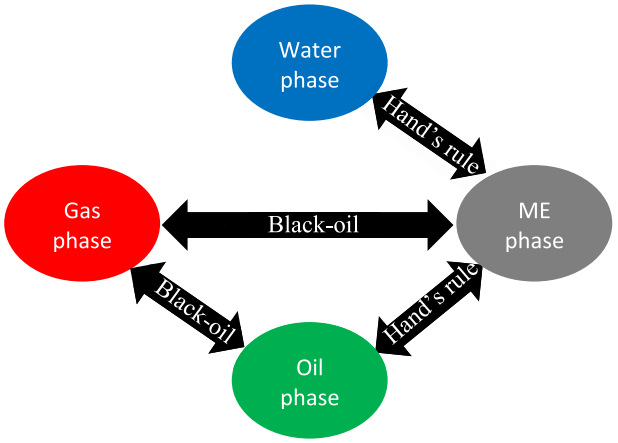

Figure 1. Four-phase coupling scheme in UTCHEM for an oil−water−gas−ME system. ME stands for microemulsion.

how the equilibrium between several phases is calculated for an oil−water−gas−microemulsion system. Table S.I.7 (see the Supporting Information) gives an overview of all of the main physical property input parameters per injection stage per simulation.

3. RESULTS AND DISCUSSION

3.1. Geochemical Reactions. EQBATCH, the geochemical module of UTCHEM, was used to obtain initial equilibrium concentrations of various components within the aqueous phase. It describes geochemical reactions that occurred in the sandstone core during the flooding processes. These initial conditions, of the components within the aqueous phase, serve as an input for the final UTCHEM model. To set up the geochemical model, the rock's mineralogical composition, together with the formation water composition, should be considered. Ion-exchange reactions with rock minerals, soap generation, dissolution/precipitation reactions, and aqueous phase reactions are crucial features for the numerical simulation of surfactant-based flooding. In this section, we discuss the geochemical model related to simulation 2 (Table 1).

The formation water considered contains the following components: 2.0 weight percent (wt %) sodium chloride (NaCl) and small amounts of calcium and carbonate ions (Ca^{2+} and CO_3^{2-}, respectively) that were emitted from the calcite mineral (carbonate minerals in Table 2) as a result of the following dissolution reactions:

Table 2. Mineralogical Composition of a Bentheimer Sandstone Core[36] [a]

quartz	feldspar	clay minerals	carbonate minerals	other
91.70	4.86	2.68	0.41	0.35

[a]The numbers represent weight percentages (wt %).

$$CaCO_3 \leftrightarrow Ca^{2+} + CO_3^{2-} \quad \text{with } K_1^{dis} = 4.95 \times 10^{-10} \tag{1}$$

$$Ca(OH)_2 \leftrightarrow Ca^{2+} + 2OH^- \quad \text{with } K_2^{dis} = 4.73 \times 10^{22} \tag{2}$$

Moreover, we considered the following aqueous reactions:

$$H_2O \leftrightarrow H^+ + OH^- \quad \text{with } K_1^{eq} = 1.00 \times 10^{-14} \tag{3}$$

$$H^+ + CO_3^{2-} \leftrightarrow HCO_3^- \quad \text{with } K_2^{eq} = 2.14 \times 10^{10} \tag{4}$$

$$2H^+ + CO_3^{2-} \leftrightarrow H_2CO_3 \quad \text{with } K_3^{eq} = 3.98 \times 10^{16} \tag{5}$$

$$Ca^{2+} + H_2O \leftrightarrow Ca(OH)^+ + H^+ \quad \text{with } K_4^{eq} = 1.21 \times 10^{-13} \tag{6}$$

$$Ca^{2+} + H^+ + CO_3^{2-} \leftrightarrow Ca(HCO_3)^+ \quad \text{with } K_5^{eq} = 1.41 \times 10^{11} \tag{7}$$

$$Ca^{2+} + CO_3^{2-} \leftrightarrow CaCO_{3(a)} \quad \text{with } K_6^{eq} = 1.58 \times 10^{3} \tag{8}$$

The abovementioned equilibrium constants (K) were obtained from the MINTEQ thermodynamic database.[34,35]

From Table 2, it can be concluded that the rock type used consists mainly of quartz minerals. However, a small amount of clay minerals are present; e.g., kaolinite. The presence of kaolinite, which is a weathering product of feldspars, implies the manifestation of the interchange between a cation in solution and another cation on the clay's surface (i.e., cation-exchange reactions). As Ca^{2+}, CO_3^{2-}, sodium ions (Na^+), and hydrogen ions (H^+) are all present in the formation water, the following cation-exchange reactions are considered:

$$2Na^+_{ads} + Ca^{2+} \leftrightarrow 2Na^+ + Ca^{2+}_{ads} \quad \text{with } K_1^{ex} = 2.62 \times 10^2 \tag{9}$$

$$H^+_{ads} + Na^+ + OH^- \leftrightarrow Na^+_{ads} + H_2O \quad \text{with } K_2^{ex} = 1.46 \times 10^7 \tag{10}$$

The exchange constants were taken from the literature.[37] The exchange capacity of the rock was assumed to be 0.047 mEq/mL.[38] It determines the amount of cations that can be adsorbed onto the rock. Exchange reactions of Na^+ and Ca^{2+} with clays are relevant to FACF since each cation in solution may have a different effect, with varying magnitude, on the phase behavior and IFT of a specific oil−water−surfactant system.[56−60] Note that potential cation-exchange reactions with surfactant micelles, which can have a significant effect on the cations present in solution,[60] were neglected. In the aforementioned

https://dx.doi.org/10.1021/acs.iecr.9b06356
Ind. Eng. Chem. Res. 2020, 59, 3606−3616

geochemical model, the following assumptions were made: (a) dissolution of quartz was assumed to be negligible as the experiment was performed at room temperature,[39] (b) in situ generation of soap was ignored as the model oil used did not contain any naphthenic acids, and (c) the major cause of alkali loss was assumed to be the cation exchange between Na^+ and H^+. The EQBATCH output file defines new initial component concentrations of the formation water: the initial conditions for chemical EOR.

3.2. Model Setup: Grid Size, Porosity, Permeability, and Initial Water Saturation. For setting up the mechanistic model, for the aid of history-matching previously performed experiments, we assume a one-dimensional displacement with the amount of grid blocks in the x-direction equal to one-fourth of the amount of computed tomography (CT) slices taken (simulations 2−6). For simulation 1, we set the amount of grid blocks in the z-direction equal to 100, as the corresponding experiment was conducted vertically. The porosity and absolute permeability values assigned to each grid block in simulation 1 were constant for each block and correspond to 23.59% and 2.23 Darcy, respectively.[9] For simulations 2−6, porosity values were calculated per CT slice (more information on CT processing is given elsewhere[9]), averaged over four consecutive CT slices, and finally assigned to a grid block. To allocate an absolute permeability value to each grid block, in simulations 2−6, the Carman−Kozeny equation, which relates porosity to absolute permeability (k), was used:[40,41]

$$k = \frac{D_p{}^2 \varphi^3}{a(1-\varphi)^2} \tag{11}$$

where D_p, ϕ, and a represent the average grain diameter in m, the porosity, and a constant factor to account for tortuosity, respectively. An averaged grain size diameter of 0.27 mm was used.[36] The tortuosity factor was estimated by solving eq 11 for the core sections over which we measured the sectional pressure drop,[9,26] using the averaged porosity, based on CT processing, and absolute permeability to brine, derived using Darcy's law,[42] for that specific section. Finally, eq 11 was used for estimating the absolute permeability values for each grid block separately. Figure 2 gives an overview of a fine cell (original CT scan discretization), course cell (simulation grid block), and core section (distance between two consecutive pressure gauges). The initial saturation conditions per grid cell at each injection phase were obtained by a standard restart procedure. At the start of the experiments, i.e., prior to oil injection (primary drainage), all grid blocks contained a water saturation (S_w) of 100%. For the following injection stages, the output of the previous injection phase was used as an input for the current injection stage for all dependent variables. During the mechanistic modeling of the various EOR injection strategies assessed, the following assumptions were made: (a) rock compressibility is negligible, (b) there is no wettability alteration, (c) fluids are incompressible, and (d) rock is strongly water-wet. Tables S.I.1−S.I.6 (see the Supporting Information) present an overview of the basic simulation parameters used per injection stage per simulation.

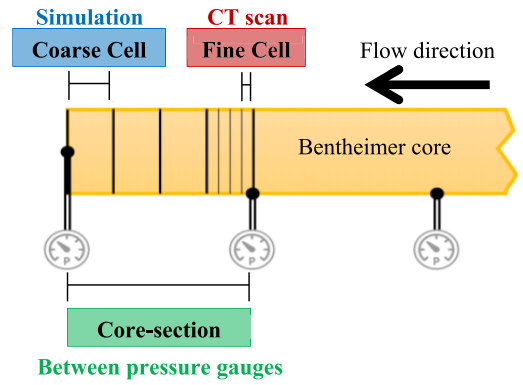

Figure 2. Relationship between core section, coarse cell, and fine cell. At first, the tortuosity factor is estimated for each core section, over which we know the absolute permeability, using an averaged porosity over multiple fine cells. Next, we used this tortuosity constant, in combination with an averaged porosity over four fine cells, to obtain absolute permeability values for each simulation grid block, i.e., for each coarse cell.

3.3. Primary Drainage and Forced Imbibition. To history-match pressure drops and saturation distributions during primary drainage and waterflooding, it is crucial to select correct relative permeability (k_r) functions for both the aqueous (k_{rw}) and oleic (k_{ro}) phases. Figures S.I.1−S.I.6 (see the Supporting Information) present an overview of the k_r curves, and parameters, used for simulating primary drainage and forced imbibition, i.e., waterflooding, in all simulations performed. In this section, we only highlight simulation 3 as it is prototypical of all mechanistic models constructed. Figure 3 presents the relative permeability curves used for simulating primary drainage and forced imbibition in simulation 3. The curves were constructed using the Corey-type[43] functions shown in Figure S.I.1. Oil and water end-point relative permeabilities ($k_{ro}{}^0$ and $k_{rw}{}^0$, respectively) were obtained by extrapolating the $k_{ro}{}^0$ and $k_{rw}{}^0$, measured in the core midsections, to the lowest water saturation measured at the end of the primary drainage (for $k_{ro}{}^0$) and to the highest water saturation observed after waterflooding (for $k_{rw}{}^0$). Residual saturations, required as an input for the Corey-type functions, were all measured in the laboratory.

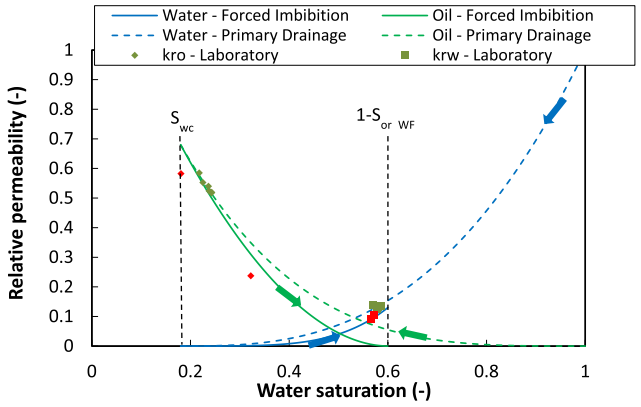

Figure 3. Relative permeability curves for the aqueous (blue) and oleic (green) phases during primary drainage (dashed lines) and waterflooding (continuous lines) used for simulation 3. The red diamonds and squares are the calculated relative permeabilities at the inlet and outlet sections of the core. They are considered to be outliers due to the tubing effect. S_{wc} and S_{or_WF} represent the connate water saturation and the residual oil saturation to waterflood, respectively.

During primary drainage, i.e., oil injection, the wetting phase saturation decreased from 1.00 to an S_{wc} of 0.18. The displacement of brine by oil followed the blue dashed line downward and the green dashed line upward until it reached S_{wc} (Figure 3). This is the starting point of waterflooding, i.e., forced imbibition. During waterflooding, water displaces oil and

https://dx.doi.org/10.1021/acs.iecr.9b06356
Ind. Eng. Chem. Res. 2020, 59, 3606−3616

reduces the nonwetting phase saturation according to the continuous green line downward and the continuous blue line upward until S_{or_WF} is reached (Figure 3).

Simulated pressure drops, phase cuts, and saturation profiles were compared with the results obtained from the laboratory. Figure 4 shows a good match between measured pressure drops

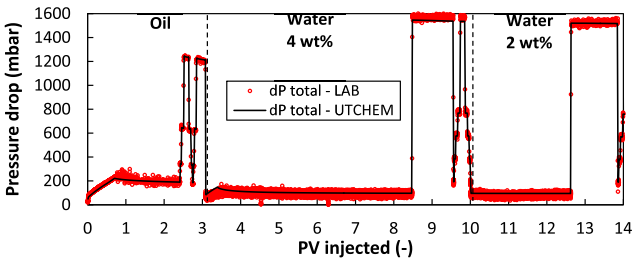

Figure 4. Simulated and measured total pressure drop (dP total) profiles for primary drainage (oil) and waterflooding (water) for simulation 3. Approximately 3.0 pore volume (PV) of oil was injected prior to waterflooding.

in the laboratory and corresponding simulated pressure drops, for both primary drainage and waterflooding. As soon as drainage was initiated, pressure drops gradually increased until oil breakthrough occurred. Afterward, a plateau value was reached. The exact same behavior in pressure drop was seen during waterflooding. Note that flow rates were varied at the end of each injection stage[9,26] to estimate k_{ro}^0 and k_{rw}^0.

Figure 5 presents the simulated and processed oil saturation (S_o) profiles as a function of distance from the inlet for both

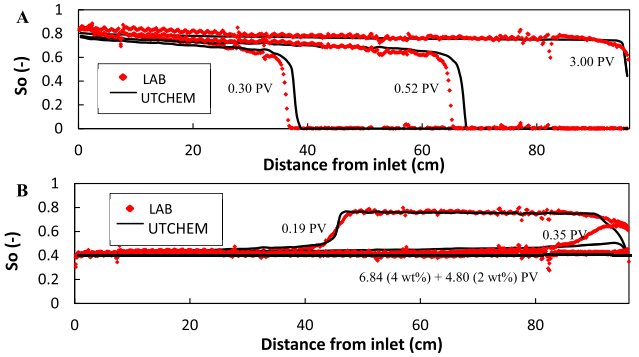

Figure 5. Oil saturation profiles obtained from experimental data and simulation for (A) primary drainage and (B) waterflooding in simulation 3.

primary drainage and waterflooding in simulation 3. The profiles for oil injection show the typical Buckley–Leverett displacement behavior, including a shock front region with a rarefaction wave upstream of it.[44] Eventually, an initial oil saturation (S_{oi}) of 0.76 ± 0.03 was reached in the simulation, which is very similar to the measured S_{oi} of 0.78 ± 0.04.[26] Note that the simulated positions of the displacement fronts (0.30 and 0.52 PV) are located somewhat more downstream compared to our observations. The latter yielded an oil breakthrough time of 0.71 PV, 0.04 ± 0.02 PV earlier compared to experimental data. The simulated saturation profiles for waterflooding (Figure 5B) show a similar behavior to that for primary drainage (Figure 5A). Although we could capture the location of the displacement front at 0.19 PV injected very well, water breakthrough happened 0.04 ± 0.02 PV earlier in the simulation compared to our observations. An S_{or_WF} of 0.40 ± 0.01 was reached in the simulation, which corresponds well with the measured one of 0.41 ± 0.02.[26] Figure 6 presents the measured and simulated

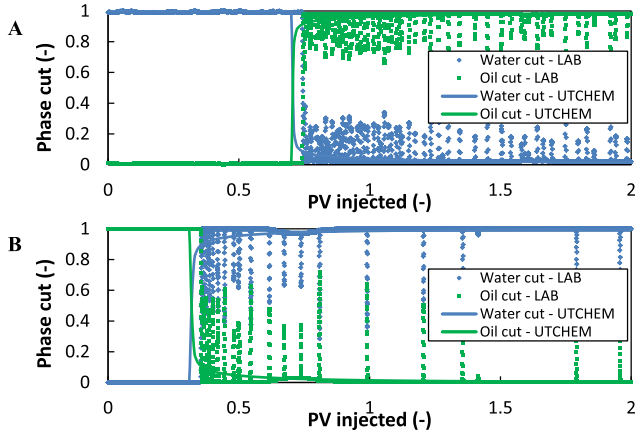

Figure 6. Comparison between measured and simulated phase cuts during (A) primary drainage and (B) waterflooding in simulation 3.

phase cuts during both injection stages. Figures S.I.7–S.I.11 (see the Supporting Information) present the observed and simulated pressure drops, S_o profiles (if available), and phase cuts (if available) for simulations 1–2 and 4–6 during primary drainage and forced imbibition.

The results presented in Figures 4 and 5 were obtained by using variable porosity and permeability values as a function of location in space (Section 3.2). When compared with using one fixed value for porosity and permeability for all locations in space, no major differences in terms of pressure drop and saturation profiles were observed. The reason for this is most probably the homogeneous nature of the Bentheimer sandstone used.

3.4. WAG Injection. After the mechanistic modeling of primary drainage, WAG flooding was simulated for simulation 1 (Table 1). To do so, it is essential to select appropriate k_r functions for the three-phase system present in the simulation. Figures S.I.12–S.I.14 (see the Supporting Information) present an overview of the k_r curves used as an input for the mechanistic modeling of WAG injection at S_{oi}. Figure 7 presents the gas

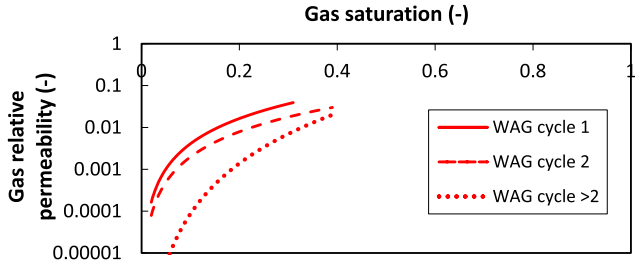

Figure 7. k_{rg} curves used as an input for simulating WAG injection in simulation 1.

relative permeability (k_{rg}) curves used for simulating WAG injection. It clearly indicates that, to properly match our experimental observations, k_{rg} needs to be reduced as a function of increasing WAG cycles (each cycle consists of the injection of a gas slug followed by a water slug). The latter seems to support the statement made in our earlier work:[9] the establishment of a

https://dx.doi.org/10.1021/acs.iecr.9b06356
Ind. Eng. Chem. Res. 2020, 59, 3606–3616

trapped gas saturation (S_{gt}) reduced gas mobility in subsequent WAG cycles.

Figure 8 presents the observed and simulated pressure drops, phase cuts, and oil recovery history for simulation 1. An excellent

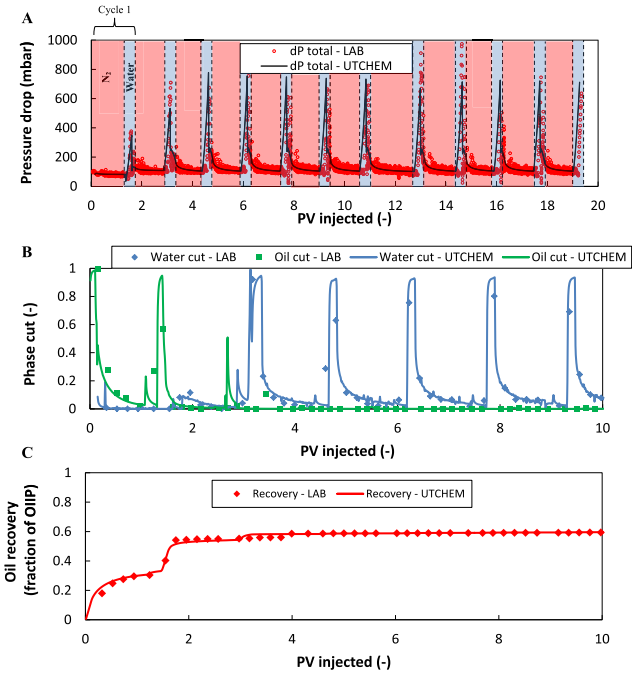

Figure 8. (A) Simulated and measured total pressure drop profiles, (B) oil and water cut, and (C) oil recovery during WAG injection at S_{oi} (simulation 1). Oil recoveries are expressed as a fraction of the oil initially in place. The red and blue schemes used in (A) refer to the injection of N_2 and water, respectively. Each WAG cycle consists of the injection of a gas slug alternated by a water slug.

match was obtained between the simulated and measured pressure drops. The sharp increase in pressure drop due to the shift from gas to water injection obtained from the experiments[9] was correctly reproduced by the simulations. The latter is the combined result of an increasing injection rate as soon as the water slug is injected and the reduced k_{rg} as a function of the increasing WAG cycles (Figure 7). The higher steady-state pressure drop simulated for gas injection during the second WAG cycle, compared to the first WAG cycle, is due to the reduced k_{rg} (i.e., presence of S_{gt}) in combination with the introduced water phase in the previous cycle. In general, a good match between the measured and simulated phase cuts (Figure 8B) was achieved. However, simulation results show a peak in oil cut at approximately 2.7 PV injected, whereas experimental observations suggest the presence of this peak at a later stage (roughly at 3.5 PV injected). The oil recovery plot (Figure 8C) clearly shows a reasonably good match between experimental observations and simulation results. The data noticeably shows that the bulk of the oil was produced throughout the first two WAG cycles.

3.5. Surfactant Phase Behavior Simulation. A detailed phase behavior model is one of the key aspects of simulating surfactant flooding in UTCHEM. The relevant phase behavior model parameters for the different phases, i.e., aqueous, oleic, and microemulsion phases, can be obtained by fitting the available models to the oil and water solubilization ratios obtained from the laboratory. The solubilization ratio of phase l is given by the ratio of the concentration of phase l solubilized in the microemulsion to the concentration of the surfactant present in the microemulsion:

$$R_{l3} = \frac{C_{l3}}{C_{33}} \qquad \text{for } l = 1 \text{ (water)}, 2 \text{ (oil)} \tag{12}$$

where R_{l3}, C_{l3}, and C_{33} are, respectively, the solubilization ratio, the concentration of phase l solubilized in the microemulsion, and the surfactant concentration solubilized in the microemulsion. A salinity scan was conducted to assess the ability of the surfactant concentration used to lower the o/w IFT at various salinities of the aqueous phase. Its result, together with the simulated solubilization ratios, is shown in Figure 9. Several

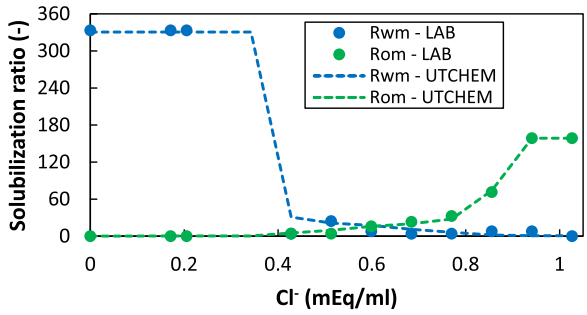

Figure 9. Simulated water (R_{wm}) and oil (R_{om}) solubilization ratios compared with the measured ones in the laboratory as a function of mEq Cl^-/mL water. Simulated solubilization ratios were used as an input for modeling (foam-assisted) chemical flooding in simulations 2–6.

simulations were performed under batch mode using model reservoir parameters to model the phase behavior of our oil–water–surfactant system (Table 3). UTCHEM uses Hand's

Table 3. Reservoir Properties and Phase Behavior Model Parameters Used

parameter	value
simulation time (days)	350
permeability (Darcy)	1000
porosity (%)	100
height of the binodal curve at zero salinity (HBNC70)	0.061
height of the binodal curve at optimal salinity (HBNC71)	0.030
height of the binodal curve at twice optimal salinity (HBNC72)	0.061
lower effective salinity (mEq/mL) (CSEL7)	0.540
upper effective salinity (mEq/mL) (CSEU7)	1.070

model[33] to represent phase behavior. The height of the binodal curve (HBNC), and the lower (CSEL) and upper (CSEU) effective salinities are used to solve the model. These parameters can be found by matching the experimental phase behavior data. As the salinity scan performed used an o/w ratio of 1:2, phase behavior simulations were carried out using 33/67 vol % oil and water concentrations, respectively. Water and oil viscosities were set at 1.0 cP. Water, oil, surfactant, and cosolvent were co-injected for several PV to reach steady-state flow, which represents the equilibrium conditions in the salinity scan conducted in the laboratory. More detailed information on the experimental procedure used to perform the salinity scan can be found elsewhere.[9,26] The used reservoir properties and phase behavior parameters (HBNCs, CSEL, and CSEU) are shown in Table 3. Figure 9 presents the final simulated solubilization ratios with the ones estimated in the laboratory.

https://dx.doi.org/10.1021/acs.iecr.9b06356
Ind. Eng. Chem. Res. 2020, 59, 3606–3616

The match between simulated and estimated solubilization ratios is fairly good. The computed optimum salinity range occurs between 0.43 and 0.77 mEq Cl^-/mL water for the oil−water−surfactant system assessed (Section 2.3), which is in good agreement with the experimental data. The curves representing R_{wm} and R_{om} cross at optimum salinity and yield a solubilization ratio of roughly 16. Using Huh's empirical correlation,[47] this solubilization ratio corresponds to an IFT on the order of 1×10^{-3} mN/m.

3.6. Surfactant Adsorption, Microemulsion Viscosity, and IFT Parameters. Surfactant adsorption was modeled in UTCHEM using a Langmuir-type isotherm, which is a function of surfactant concentration, salinity, and rock permeability.[45] It is given by

$$\hat{C}_3 = \min\left(\hat{C}_3, \frac{a_3(\dot{C}_3 - \hat{C}_3)}{1 + b_3(\dot{C}_3 - \hat{C}_3)}\right),$$
$$a_3 = (a_{31} + a_{32}C_{SE})\left(\frac{k_{ref}}{k}\right)^{0.5} \quad (13)$$

where $\hat{C}_3$ is the adsorbed concentration of the surfactant, and $\dot{C}_3$ represents the total surfactant concentration. Adsorption parameters a_3 and b_3 can be found by matching laboratory data, if available. The minimum is taken to ensure that the adsorbed concentration does not exceed the total surfactant concentration. Surfactant adsorption increases linearly with effective salinity (C_{SE}) and decreases with increasing permeability (k). All input parameters (a_{31}, a_{32}, and b_3) need to be specified at a reference permeability (k_{ref}). Since we did not measure the amount of surfactant that remained in the core during surfactant flooding in the performed FACF core-floods, we used the average surfactant adsorption in the Bentheimer sandstones measured earlier[23] for the same type of surfactant slug: 0.25 ± 0.12 mg/g rock. Note that this value for surfactant retention lies within the ranges measured by others who performed surfactant retention measurements for a large number of cores.[46] Initially, model parameters were chosen that match the average surfactant adsorption of 0.25 mg/g rock. At a later stage, parameters were tuned to obtain a better match for the pressure drop and saturation profiles, while ensuring that the surfactant adsorption remained within its boundaries (0.25 ± 0.12 mg/g rock). Figure S.I.15 (see the Supporting Information) presents the final Langmuir-type adsorption isotherm that was used in simulation 2.

The viscosity of the microemulsion generated during the core-floods could not be measured. Therefore, the microemulsion viscosity as a function of aqueous phase salinity was initially determined using default parameters. Microemulsion viscosity parameters were adjusted, if needed, until a good match between measured and simulated pressure drops, and S_o profiles, was obtained. The resulting microemulsion viscosity that was used in the mechanistic model equaled 1.41 cP (simulations 2−5) or 1.67 cP (simulation 6).

To estimate microemulsion/oil and microemulsion/water IFTs, a modified version of Huh's relationship[47] was used:

$$\sigma_{l3} = \sigma_{ow}e^{-aR_{l3}} + \frac{cF_l}{R_{l3}^2}(1 - e^{-aR_{l3}^3})$$
$$\text{for } l = 1(\text{water}),\ 2(\text{oil}) \quad (14)$$

where σ_{l3}, σ_{ow}, and R_{l3} represent the phase l/microemulsion IFT in mN/m, the o/w IFT in the absence of surfactant (roughly 24 mN/m), and the solubilization ratio of phase l in phase 3 (eq 12), respectively. Equation 14 uses Hirasaki's correction factor, F_l, to ensure that the IFT equals zero at the plait point.[48] The abovementioned equation contains two matching parameters, c and a, which were set to 0.1 (c) and 20 (a) for all simulations.

3.7. Relative Permeability Surfactant Flooding. For history-matching measured pressure drops, phase cuts, and S_o profiles, the k_r curves for both oil and water, at the respective salinity conditions during surfactant slug injection, are crucial. To construct such k_r curves, the Corey-type functions[43] are used, similar to the simulation of primary drainage and forced imbibition (Section 3.3). For modeling k_r for surfactant flooding, UTCHEM assumes that, at miscible conditions, zero o/w IFT is achieved.[49] This assumption implies that, at miscible conditions, k_{ro}^0 and k_{rw}^0, as well as the Corey exponents, are unity, and the corresponding residual oil and water saturations equal zero. The k_{ro} and k_{rw} curves at under-optimum salinity surfactant injection are constructed by interpolating the k_r curves between forced imbibition (Figures S.I.2−S.I.6 in the Supporting Information) and the aforementioned miscible conditions. Figure 10 presents the representative k_{ro} and k_{rw} curves for forced imbibition (i.e., low trapping number), for miscible conditions (i.e., high trapping number), and for the under-optimum salinity conditions imposed in simulation 2 (used for simulating surfactant slug injection). Figures S.I.16−S.I.19 (see the Supporting Information) present the k_{ro} and k_{rw} curves used for the mechanistic modeling of surfactant slug injection in simulations 3−6.

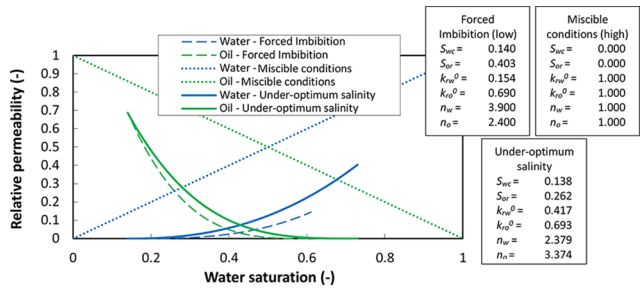

Figure 10. Oil and water relative permeability curves for forced imbibition, 100% miscibility, and for under-optimum salinity flooding in simulation 2. The curves for under-optimum salinity are used as input in the simulation. The relative permeabilities are modeled using the Corey-type functions shown in Figure S.I.1 (see the Supporting Information). Forced imbibition refers to a so-called low trapping number, whereas a high trapping number represents miscible conditions.

3.8. Oil Mobilization by Surfactant Slug Injection. Once all aforementioned parameters were implemented in the UTCHEM model, simulated pressure drops and S_o profiles, for surfactant slug injection, were compared with the experimental results acquired in the laboratory. In this section, we focus on simulations 3 and 6 to shed light on the effect of salinity on oil mobilization during surfactant slug injection. Figure 11 presents an overview of the measured and simulated pressure drops and S_o profiles for surfactant slug injection in simulations 3 (under-optimum salinity) and 6 (near-optimum salinity). Phase cuts and the oil recovery history are not shown since no oil was recovered during the slug injection of approximately 0.46 PV. Figures S.I.20−S.I.22 (see the Supporting Information) present the simulation results, during surfactant slug injection, for all other simulations. Note that the

https://dx.doi.org/10.1021/acs.iecr.9b06356
Ind. Eng. Chem. Res. 2020, 59, 3606−3616

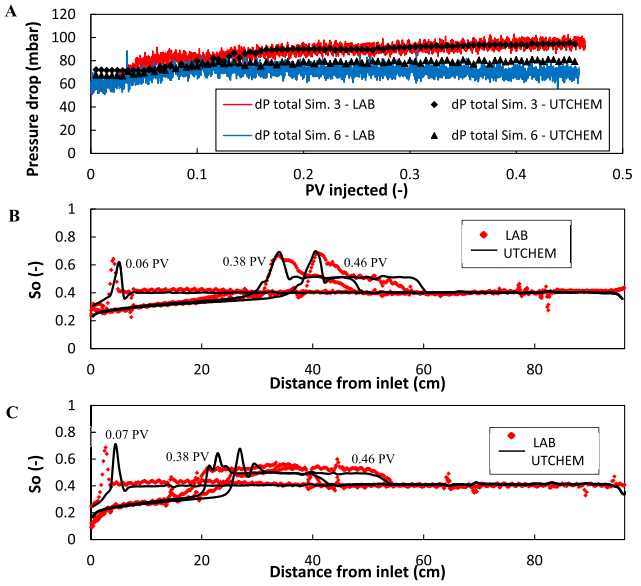

Figure 11. (A) Simulated and measured total pressure drop profiles for the surfactant slug injection stage in simulations 3 and 6, (B) oil saturation profiles obtained from experimental data and simulation for slug injection in simulation 3, and (C) oil saturation profiles obtained from experimental data and simulation for slug injection in simulation 6.

latter includes the mechanistic simulation of the baseline coreflood discussed in our previous work,[26] i.e., extended surfactant flooding (simulation 2 in Table 1).

To confirm the robustness of the phase behavior model presented in Section 3.5, we applied it to the two different salinity conditions used in simulations 3 and 6 (Table 1). Figure 11A shows a fairly good match between simulated and observed pressure drops for both cases. We were able to capture the gradually increasing trend in pressure drop, as a function of PV injected, in simulation 3, whereas simulation 6 shows a fairly constant pressure drop as a function of injection time, similar to related experimental observations.[9] The S_o profiles corresponding to simulation 3 (Figure 11B) show, in general, a satisfactory match with the related experimental observations. Peak S_o values within the generated oil bank were successfully matched, especially for later injection times (i.e., 0.38 and 0.46 PV). Although experimental results indicate that, as injection continued, the oil bank became more dispersed [shown by the gradual reduction of S_o on the leading edge (i.e., downstream side)], this phenomenon was hard to capture in the model. The S_o profiles constructed with the UTCHEM model exhibit a more uniform structure of the banked oil at its leading edge compared to the experimental observations. The constructed S_o profiles related to simulation 6 (Figure 11C) show a reasonable match with the corresponding laboratory results. The propagation of the oil bank's leading edge was perfectly matched at injection times of 0.38 and 0.46 PV. At early injection times, i.e., at 0.07 PV, there is a small gap in the location of the oil bank between observed and simulated data. Although here we observed a uniform shape of the oil bank in the laboratory, at later injection times, corresponding simulation results indicate a more dispersed character of the oil accumulation at its trailing edge (i.e., upstream side). Note that the match in simulation 6 required a slight increase in surfactant adsorption due to an increased aqueous phase salinity, which is in agreement with the literature.[50]

3.9. Displacement of Mobilized Oil by Foam. The local equilibrium foam model in UTCHEM is based on the work of Cheng.[49,51] It uses the following parameters to control foam generation: (a) the surfactant concentration within the aqueous phase (C_s) needs to exceed a threshold concentration (C_s*), (b) S_w needs to exceed a threshold saturation (S_w*), and (c) S_o should not be higher than a critical oil saturation (S_o*). The foam model used here assigns the reduction in gas mobility, due to foam generation, fully to the reduction in k_{rg}.[49,52] The first two threshold parameters (C_s* and S_w*) affect k_{rg} as follows

$$k_{rg}^{f} = \begin{cases} k_{rg} & S_w < S_w^* - \varepsilon \text{ or } C_s < C_s^* \\ \dfrac{k_{rg}}{1 + \dfrac{(R-1)(S_w - S_w^* + \varepsilon)}{2\varepsilon}} & S_w^* - \varepsilon \le S_w \le S_w^* + \varepsilon \text{ and } C_s \ge C_s^* \\ \dfrac{k_{rg}}{R} & S_w > S_w^* + \varepsilon \text{ and } C_s \ge C_s^* \end{cases} \quad (15)$$

where k_{rg}^{f}, ε, and R represent the effective gas relative permeability modified for the presence of foam, a tolerance parameter for S_w, and the gas mobility reduction factor, respectively. The latter is given by

$$R = R_{ref}\left(\frac{u_g}{u_{g,ref}}\right)^{\sigma-1} \quad (16)$$

where R_{ref}, $u_{g,ref}$, and σ stand for the reference gas mobility reduction factor, the reference gas velocity at which R_{ref} is calculated, and a power-law exponent, respectively. Equation 16 indicates that R is modified according to the gas flow rate to allow for the shear-thinning behavior of foam in the low-quality regime.[49] The model implies that foam cannot be formed at $S_o > S_o$*.

To assess whether the local equilibrium foam model in UTCHEM can potentially be used for reproducing our experimental observations discussed in our earlier work,[9,26] first we need to recapitulate the interpretation of the experimental results. As discussed in the earlier study,[26] in the case of a 57 and 77% drive foam quality (simulations 3 and 4), the obtained pressure drop data and gas saturation (S_g) profiles indicate foaming characteristics to occur in an area with relatively high S_o, which are remnants of the oil bank. The suggested mechanism includes a reduction in effective porosity (i.e., part of the total porosity that contributes to fluid flow), increased gas and liquid interstitial velocities, and, consequently, an increased local pressure gradient, which might be the trigger for foam generation.[9,26,53] The aforementioned foam model in UTCHEM is not in line with our experimental observations and the suggested mechanism, since it entails the complete collapse of foam at $S_o > S_o$*. It involves foam destruction as a function of increasing S_o, whereas laboratory investigation suggested foam generation being promoted in an area with relatively high S_o. The latter indicates that the local equilibrium foam model within UTCHEM is not suitable for simulating the foam generation mechanism observed in our experiments.

For testing purposes, we tried to use the model in an inconvenient, nonphysical, way for reproducing our experimental results in simulation 3. For this purpose, we propose to use variable S_w*, i.e., the value of S_w at which foam will collapse, as our controlling parameter. The parameter S_w* was predefined at each local grid block (Figure 2), based on measured S_g profiles that indicate foam generation,[9,26] to control the location at

https://dx.doi.org/10.1021/acs.iecr.9b06356
Ind. Eng. Chem. Res. 2020, 59, 3606−3616

which the foam starts to generate. By doing so, it was possible to selectively control the behavior of k_{rg}^{f}. Note that variable S_w* was, in fact, the only parameter in the foam model that could be selectively controlled. The other two threshold parameters, C_s* and S_o*, are chosen such that they allow foam generation to occur at all locations in space. Figure 12 presents the S_w* distribution for simulation 3. It was generated as follows: (a) find a function (f) that effectively reproduces the S_g profile, which is a qualitative indicator of foam generation, observed at 1.08 PV injected (see Figure S.I.23 in the Supporting Information), (b) calculate $1 - f$ to obtain the correct shape of the S_w* curve, and (c) use eq 17 in an iterative way to obtain the final S_w* curve:

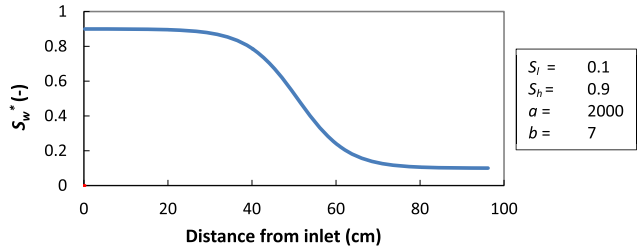

Figure 12. S_w* distribution applied in simulation 3 for the simulation of drive foam injection.

$$S_w^*{}_i = S_l + \frac{(S_h - S_l)}{1 + a(10^{(x_{Di}-1)b})} \quad (17)$$

where a and b function as fitting parameters, S_l and S_h represent the lower and higher limit values for S_w*, respectively, and x_{Di} is the dimensionless distance in the x-direction of cell i.

Figure 13 presents an overview of measured and simulated pressure drops, oil recovery, and S_o profiles for drive foam injection in simulation 3. Overall, a good representation of the pressure drop was obtained. The simulated oil recovery history corresponds perfectly well with laboratory observations. The latter implies representative modeling of the oil bank propagation, which is verified by the S_o profiles shown in Figure 13C. Similar to our experimental observations,[26] the oil bank's peak S_o was reduced as soon as co-injection of gas and surfactant solution was initiated.

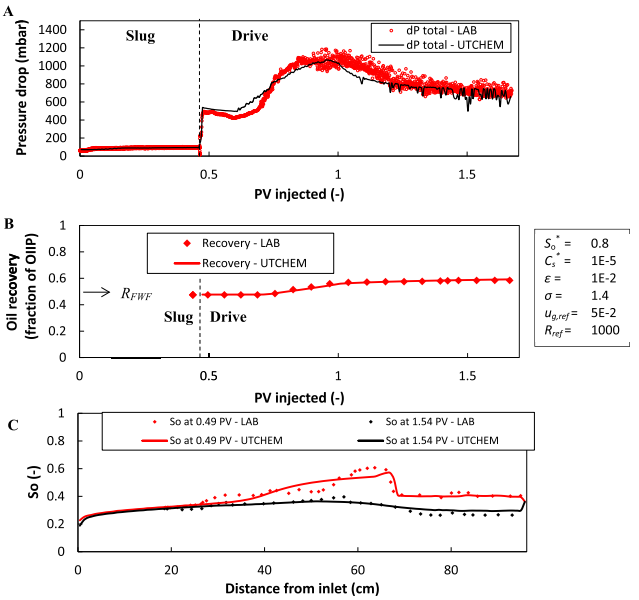

Figure 13. (A) Simulated and measured total pressure drop profiles for slug and drive foam injection in simulation 3, (B) oil recovery history as a function of OIIP, and (C) oil saturation profiles obtained from experimental data and simulation for drive foam injection in simulation 3. PV = 0 equals the start of surfactant slug injection. The table on the right-hand side presents an overview of the model parameters used (except for S_w*). Note that the extreme values for S_o* and C_s* were assumed, which allowed us to use S_w* as a controlling parameter (Figure 12). R_{FWF} represents the recovery factor for waterflooding.

4. CONCLUSIONS

A mechanistic modeling study on WAG and FACF, based on the core-flood experiments presented in our earlier work,[9,26] was conducted. An in-house three-dimensional chemical flooding research simulator (UTCHEM) for multiphase and multicomponent systems was used. The FACF core-floods were modeled by including the surfactant phase behavior as a function of salinity, fluid rheology, capillary desaturation of oil, gas mobility reduction due to foam generation, and potential essential geochemical reactions that occurred in the sandstone core. All simulations were performed under a one-dimensional configuration. This study resulted in the following main conclusions:

- Primary drainage and forced imbibition injection stages were successfully modeled. Relative permeability curves for primary drainage and forced imbibition were estimated using CT-scan-based saturation distributions in combination with effective permeability measurements based on sectional pressure drops in the core.
- History-matching WAG injection revealed that a reduction in k_{rg} was required as a function of increasing WAG cycles. This, most likely, verifies the effect of the establishment of a trapped, i.e., immobile, gas saturation. Similar to our experimental results, the bulk of the oil was produced during the injection of the first two WAG cycles.
- The surfactant phase behavior for our experimental conditions was successfully modeled. The robustness of the model was verified by effectively applying the same phase behavior model to the two different salinity conditions studied. Moreover, we were able to identify the correct trapping number parameters to acquire representative water and oil relative permeability curves for low o/w IFT flooding. This laid a solid foundation for the proper modeling of oil mobilization due to surfactant slug injection.
- Although UTCHEM was demonstrated to be a useful simulation tool, able to represent complex phenomena involved in a four-phase system, its local equilibrium foam model was not able to cover a wide range of possible foam generation mechanisms. To overcome this drawback, we introduced a selectively controlled S_w*.

■ ASSOCIATED CONTENT

Supporting Information

The Supporting Information is available free of charge at https://pubs.acs.org/doi/10.1021/acs.iecr.9b06356.

Simulation parameters used per injection stage per simulation (Tables S.I.1−S.I.6); relative permeability curves: primary drainage and forced imbibition (Figures S.I.1−S.I.6); pressure drops, oil saturation profiles, and phase cuts: primary drainage and forced imbibition

https://dx.doi.org/10.1021/acs.iecr.9b06356
Ind. Eng. Chem. Res. 2020, 59, 3606−3616

(Figures S.I.7−S.I.11); relative permeability curves: WAG injection (Figures S.I.12−S.I.14); Langmuir-type adsorption isotherm used for modeling surfactant adsorption in simulation 2 (Figure S.I.15); relative permeability curves: surfactant slug injection (Figures S.I.16−S.I.19); pressure drops and oil saturation profiles: surfactant slug injection (Figures S.I.20−S.I.22); gas saturation profiles during foam drive injection in the FACF experiment to be simulated in simulation 3 (Figure S.I.23); overview of main physical property input parameters used for each injection stage per simulation (Table S.I.7) (PDF)

AUTHOR INFORMATION

Corresponding Author

Martijn T. G. Janssen − *Petroleum Engineering Department, Delft University of Technology 2628 CN Delft, The Netherlands;* orcid.org/0000-0002-0940-4998; Email: mjanssen2@outlook.com

Authors

Fabian A. Torres Mendez − *Petroleum Engineering Department, Delft University of Technology 2628 CN Delft, The Netherlands*

Pacelli L. J. Zitha − *Petroleum Engineering Department, Delft University of Technology 2628 CN Delft, The Netherlands*

Complete contact information is available at: https://pubs.acs.org/10.1021/acs.iecr.9b06356

Notes

The authors declare no competing financial interest.

ACKNOWLEDGMENTS

This study is the result of a collaboration between the Delft University of Technology, Universiti Teknologi Petronas, Petronas, and Shell. The authors are grateful to Petronas and Shell for funding the project. The authors thank the Center for Petroleum and Geosystems Engineering at the University of Texas at Austin, Texas for allowing them to use their chemical simulator UTCHEM.

REFERENCES

(1) Höök, M.; Hirsch, R.; Aleklett, K. Giant oil field decline rates and their influence on world oil production. *Energy Policy* **2009**, *37*, 2262−2272.

(2) Zhu, T.; Ogbe, D. O.; Khataniar, S. Improving the foam performance for mobility control and improved sweep efficiency in gas flooding. *Ind. Eng. Chem. Res.* **2004**, *43*, 4413−4421.

(3) Rossen, W. R.; Van Duijn, C. J.; Nguyen, Q. P.; Vikingstad, A. K. Injection Strategies to Overcome Gravity Segregation in Simultaneous Gas and Liquid Injection into Homogeneous Reservoirs. *SPE J.* **2010**, *15*, 76−90.

(4) Farajzadeh, R.; Andrianov, A.; Bruining, J.; Zitha, P. Comparative Study of CO2 and N2 Foams in Porous Media at Low and High Pressure-Temperatures. *Ind. Eng. Chem. Res.* **2009**, *48*, 4542−4552.

(5) Farajzadeh, R.; Andrianov, A.; Zitha, P. Investigation of Immiscible and Miscible Foam for Enhancing Oil Recovery. *Ind. Eng. Chem. Res.* **2010**, *49*, 1910−1919.

(6) Andrianov, A. I.; Liu, M. K.; Rossen, W. R. In *Sweep Efficiency in CO2 Foam Simulations With Oil*, Presented at the SPE EUROPEC/EAGE Annual Conference and Exhibition, SPE-142999-MS, Vienna, Austria, May 23−26, 2011. https://doi.org/10.2118/142999-MS.

(7) Bhoendie, K. S.; Moe Soe Let, K. P.; Li, T.; Zitha, P. L. J. In *Laboratory Evaluation of Gas-Injection EOR for the Heavy-Oil Reservoirs in Suriname*, Presented at the SPE Heavy and Extra Heavy Oil Conference, SPE-171038-MS, Latin America, Medellin, CO, 2014. https://doi.org/10.2118/171038-MS.

(8) Talebian, S. H.; Masoudi, R.; Tan, I. M.; Zitha, P. L. J. Foam assisted CO_2-EOR: A review of concept, challenges, and future prospects. *J. Pet. Sci. Eng.* **2014**, *120*, 202−215.

(9) Janssen, M. T. G.; Pilus, R. M.; Zitha, P. L. J. A Comparative Study of Gas Flooding and Foam-Assisted Chemical Flooding in Bentheimer Sandstones. *Transp. Porous Media* **2019**, *131*, 101−134.

(10) Kovscek, A. R.; Radke, C. J. Fundamentals of Foam Transport in Porous Media. In *Foams: Fundamentals and Applications in the Petroleum Industry*; American Chemical Society: Washington, DC, 1994; Chapter 3, pp 115−163.

(11) Rossen, W. R. Foams in Enhanced Oil Recovery. In *Foams: Theory, Measurements and Applications*; Marcel Dekker Inc.: New York City, 1996; Chapter 11, pp 413−464.

(12) Zitha, P. L. J.; Nguyen, Q. P.; Currie, P. K.; Buijse, M. A. Coupling of foam drainage and viscous fingering in porous media revealed by X-ray computed tomography. *Transp. Porous Media* **2006**, *64*, 301−313.

(13) Du, D.; Zitha, P. L. J.; Uijttenhout, M. G. Carbon dioxide foam rheology in porous media: a CT scan study. *SPE J.* **2007**, *12*, 245−252.

(14) Zitha, P. L. J.; Du, D. X. A new stochastic bubble population model for foam flow in porous media. *Transp. Porous Media* **2010**, *83*, 603−621.

(15) Simjoo, M.; Dong, Y.; Andrianov, A.; Talanana, M.; Zitha, P. L. J. CT scan study of immiscible foam flow in porous media for enhancing oil recovery. *Ind. Eng. Chem. Res.* **2013**, *52*, 6221−6233.

(16) Lake, L. W. *Enhanced Oil Recovery*; Prentice-Hall: Englewood Cliffs, NJ, 1989.

(17) Gauglitz, P. A.; Friedmann, F.; Kam, S. I.; Rossen, W. R. In *Foam Generation in Porous Media*, Presented at the SPE Improved Oil Recovery Symposium, SPE-75177-MS, Tulsa, OK, April 13−17, 2002. https://doi.org/10.2118/75177-MS.

(18) Kang, W.; Liu, S.; Meng, L.; Cao, D.; Fan, H. *A Novel Ultra-Low Interfacial Tension Foam Flooding Agent to Enhance Heavy Oil Recovery*, Presented at the SPE Improved Oil Recovery Symposium, SPE-129175-MS; Tulsa, OK, April 24−28, 2010. https://doi.org/10.2118/129175-MS.

(19) Hirasaki, G. J.; Miller, C. A.; Puerto, M. Recent advances in surfactant EOR. *SPE J.* **2011**, *16*, 889−907.

(20) Guo, H.; Zitha, P. L. J.; Faber, R.; Buijse, M. A novel alkaline/surfactant/foam enhanced oil recovery process. *SPE J.* **2012**, *17*, 1186−1195.

(21) Jong, S.; Nguyen, N. M.; Eberle, C. M.; Nghiem, L. X.; Nguyen, Q. P. In *Low Tension Gas Flooding as a Novel EOR Method: An Experimental and Theoretical Investigation*, Presented at the SPE Improved Oil Recovery Conference, SPE-179559-MS, Tulsa, OK, April 11−13, 2016. https://doi.org/10.2118/179559-MS.

(22) Winsor, P. A. *Solvent Properties of Amphiphilic Compounds*; Butterworths Scientific Publications Ltd.: London, 1954.

(23) Battistutta, E.; van Kuijk, S. R.; Groen, K. V.; Zitha, P. L. J. In *Alkaline-Surfactant-Polymer (ASP) Flooding of Crude Oil at Under-Optimum Salinity Conditions*, Presented at the SPE Asia Pacific Enhanced Oil Recovery Conference, SPE-174666-MS, Kuala Lumpur, Malaysia, August 11−13, 2015. https://doi.org/10.2118/174666-MS.

(24) Hosseini-Nasab, S. M.; Zitha, P. L. J. In *Systematic Phase Behaviour Study and Foam Stability Analysis for Optimal Alkaline/Surfactant/Foam Enhanced Oil Recovery*, Presented at the 18th European Symposium on Improved Oil Recovery, EAGE, Dresden, Germany, April 14−16, 2015.

(25) Janssen, M. T. G.; Mutawa, A. S.; Pilus, R. M.; Zitha, P. L. J. Foam-Assisted Chemical Flooding for Enhanced Oil Recovery: Effects of Slug Salinity and Drive Foam Strength. *Energy Fuels* **2019**, *33*, 4951−4963.

(26) Janssen, M. T. G.; Zitha, P. L. J.; Pilus, R. M. Oil Recovery by Alkaline/Surfactant/Foam Flooding: Effect of Drive-Foam Quality on Oil-Bank Propagation. *SPE J.* **2019**, No. 190235.

(27) Goudarzi, A.; Delshad, M.; Sepehrnoori, K. In *A Critical Assessment of Several Reservoir Simulators for Modeling Chemical*

Enhanced Oil Recovery Processes, Presented at the SPE Reservoir Simulation Symposium, SPE-163578-MS, The Woodlands, TX, February 18−20, 2013. https://doi.org/10.2118/163578-MS.
(28) Lashgari, H. R.; Sepehrnoori, K.; Delshad, M.; DeRouffignac, E. In *Development a Four-Phase Chemical-Gas Model in an IMPEC Reservoir Simulator*, Presented at the SPE Reservoir Simulation Symposium, SPE-173250-MS, Houston, TX, February 23−25, 2015. https://doi.org/10.2118/173250-MS.
(29) Lashgari, H. R.; Delshad, M.; Sepehrnoori, K.; DeRouffignac, E. Development and Application of Electrical-Joule-Heating Simulator for Heavy-Oil Reservoirs. *SPE J.* **2015**, *21*, 87−100.
(30) Fortenberry, R.; Suniga, P.; Mothersele, S.; Delshad, M.; Lashgari, H.; Pope, G. A. In *Selection of a Chemical EOR Strategy in a Heavy Oil Reservoir Using Laboratory Data and Reservoir Simulation*, Presented at the SPE Canada Heavy Oil Technical Conference, SPE-174520-MS, Calgary, Alberta, Canada, June 9−11, 2015. https://doi.org/10.2118/174520-MS.
(31) Lashgari, H. R.; Sepehrnoori, K.; Delshad, M. In *Modeling of Low-Tension Surfactant-Gas Flooding Process in a Four-Phase Flow Simulator*, Presented at the SPE Annual Technical Conference and Exhibition, SPE-175134-MS, Houston, TX, September 28−30, 2015. https://doi.org/10.2118/175134-MS.
(32) Delshad, M.; Najafabadi, N. F.; Anderson, G. A.; Pope, G. A.; Sepehrnoori, K. In *Modeling Wettability Alteration in Naturally Fractured Reservoirs*, Presented at the SPE Improved Oil Recovery Symposium, SPE-100081-MS, Tulsa, OK, April 22−26, 2006. https://doi.org/10.2118/100081-MS.
(33) Hand, D. B. Dineric Distribution: I. The Distribution of a Consolute Liquid Between Two Immiscible Liquids. *J. Phys. Chem. A* **1939**, *34*, 1961−2000.
(34) Plummer, L. N.; Busenberg, E. The solubilities of calcite, aragonite and vaterite in CO2 solutions between 0 and 90 °C, and an evaluation of the aqueous model for the system CaCO3-CO2-H2O. *Geochim. Cosmochim. Acta* **1982**, *46*, 1011−1040.
(35) Nordstrom, D. K.; Plummer, L. N.; Langmuir, D.; Busenberd, E.; May, H. M.; Jones, B. F.; Parkhurst, D. L. In *Revised Chemical Equilibrium Data for Major Water-Mineral Reactions and Their Limitations*, Chemical Modelling of Aqueous Systems II: American Chemical Society Symposium Series 416, 1990; pp 398−413.
(36) Peksa, A. E.; Wolf, K. H. A.; Zitha, P. L. J. Bentheimer sandstone revisited for experimental purposes. *Mar. Pet. Geol.* **2015**, *67*, 701−719.
(37) Sheng, J. *Modern Chemical Enhanced Oil Recovery: Theory and Practice*; Gulf Professional Publishing, 2010.
(38) Hosseini-Nasab, S. M.; Padalkar, C.; Battistutta, E.; Zitha, P. L. J. Mechanistic modeling of the alkaline/surfactant/polymer flooding process under sub-optimum salinity conditions for enhanced oil recovery. *Ind. Eng. Chem. Res.* **2016**, *55*, 6875−6888.
(39) Fournier, R. O.; Rowe, J. J. The solubility of amorphous silica in water at high temperatures and high pressures. *Am. Mineral.* **1977**, *62*, 1052−1056.
(40) Kozeny, J. In *Uber kapillare leitung der wasser in boden*, Proceedings Class I, Royal Academy of Science: Vienna, 1927; pp 271−306.
(41) Carman, P. C. Fluid flow through granular beds. *Trans. Inst. Chem. Eng.* **1937**, *15*, 150−166.
(42) Darcy, H. *Les fontaines publiques de la ville de Dijon: exposition et application*; Victor Dalmont, 1856.
(43) Brooks, R. H.; Corey, A. T. Properties of porous media affecting fluid flow. *J. Irrig. Drain. Div.* **1966**, *92*, 61−90.
(44) Buckley, S. E.; Leverett, M. Mechanism of fluid displacement in sands. *Trans. AIME* **1942**, *146*, 107−116.
(45) Hirasaki, G. J.; Pope, G. A. Analysis of factors Influencing mobility and adsorption in the Flow of polymer solution through porous media. *SPE J.* **1974**, *14*, 337−346.
(46) Solairaj, S.; Britton, C.; Kim, D. H.; Weerasooriya, U.; Pope, G. A. In *Measurement and Analysis of Surfactant Retention*, Presented at the SPE Improved Oil Recovery Symposium, SPE-154247-MS, Tulsa, OK, April 14−18, 2012. https://doi.org/10.2118/154247-MS.
(47) Huh, C. Interfacial tensions and solubilizing ability of a microemulsion phase that coexists with oil and brine. *J. Colloid Interface Sci.* **1979**, *71*, 408−426.
(48) Hirasaki, G. L. Application of the theory of multicomponent, multiphase displacement to three component, two-phase surfactant flooding. *SPE J.* **1981**, *21*, 191−204.
(49) UTCHEM Technical Documentation. *Volume II Documentation for UTCHEM 2017_3: A Three-Dimensional Chemical Flood Simulator*; UTCHEM Technical Documentation, 2017.
(50) Song, F. Y.; Islam, M. R. Effect of salinity and rock type on sorption behaviour of surfactants as applied in cleaning of petroleum contaminants. *J. Pet. Sci. Eng.* **1994**, *10*, 321−336.
(51) Cheng, L.; Reme, A. B.; Shan, D.; Coombe, D. A.; Rossen, W. R. In *Simulating Foam Processes at High and Low Foam Qualities*, Presented at the SPE Improved Oil Recovery Symposium, SPE-59287-MS, Tulsa, OK, April 3−5, 2000. https://doi.org/10.2118/59287-MS.
(52) Lotfollahi, M. Development of a Four-Phase Flow Simulator to Model Hybrid Gas/Chemical EOR Processes. Ph.D. Dissertation, The University of Texas, 2015.
(53) Rossen, W. R.; Gauglitz, P. A. Percolation theory of creation and mobilization of foams in porous media. *AIChE J.* **1990**, *36*, 1176−1188.
(54) Pope, G. A. The Application of Fractional Flow Theory to Enhanced Oil Recovery. *SPE J.* **1980**, *20*, 191−205.
(55) Farajzadeh, R.; Wassing, B. L.; Lake, L. W. Insights into design of mobility control for chemical enhanced oil recovery. *Energy Rep.* **2019**, *5*, 570−578.
(56) Pope, G. A.; Lake, L. W.; Helfferich, F. G. Cation Exchange in Chemical Flooding: Part 1-Basic Theory without Dispersion. *SPE J.* **1978**, *18*, 418−434.
(57) Hill, H. J.; Helfferich, F. G.; Lake, L. W.; Reisberg, J.; Pope, G. A. Cation Exchange and Chemical Flooding. *J. Pet. Technol.* **1977**, *29*, 1−336.
(58) Lake, L. W.; Helfferich, F. Cation Exchange in Chemical Flooding: Part 2-The Effect of Dispersion, Cation Exchange, and Polymer/Surfactant Adsorption on Chemical Flood Environment. *SPE J.* **1978**, *18*, 435−444.
(59) Hill, H. J. Cation Exchange in Chemical Flooding: Part 3—Experimental. *SPE J.* **1978**, *18*, 445−456.
(60) Hirasaki, G. J. Ion Exchange with Clays in the Presence of Surfactant. *SPE J.* **1982**, *22*, 181−192.

https://dx.doi.org/10.1021/acs.iecr.9b06356
Ind. Eng. Chem. Res. 2020, 59, 3606−3616